Suppression of the magnetic moment under the action of a transverse magnetic field in hard superconductors

L. M. Fisher
All-Russian Electrical Engineering Institute, 111250 Moscow, Russia

K. V. Il'enko
Institute for Radiophysics and Electronics, NAS, 310085 Kharkov, Ukraine

A. V. Kalinov
All-Russian Electrical Engineering Institute, 111250 Moscow, Russia

M. A. R. LeBlanc
Department of Physics, University of Ottawa, Ottawa, Canada K1N 6N5

F. Pérez-Rodríguez
Instituto de Física, Universidad Autónoma de Puebla, Apartado Postal J-48, Puebla, Puebla 72570, México

S. E. Savel'ev and I. F. Voloshin
All-Russian Electrical Engineering Institute, 111250 Moscow, Russia

V. A. Yampol'skii
Institute for Radiophysics and Electronics, NAS, 310085 Kharkov, Ukraine
(Received 16 March 1999; revised manuscript received 24 January 2000)

The suppression of the static magnetic moment M of a superconducting plate in the critical state by a sweeping magnetic field $\vec{h}(t)$, applied perpendicularly to a dc magnetic field $\vec{\mathcal{H}}$, has been studied experimentally and theoretically. For every quarter-period of a sweeping field $h(t)$ of changing polarity with an amplitude h_0, a noticeable decrease of M can be observed both for the paramagnetic and diamagnetic initial states even for small h_0 compared to $\mathcal{H}$. Numerical simulations within the framework of two existing theoretical approaches have been performed in order to study the evolution of the distribution of the magnetic induction and the suppression of the magnetic moment. It turns out that the Clem–Pérez-González double critical-state model describes this process qualitatively well in the first quarter-period for relatively high values of h_0. A significant disagreement with the experimental data is observed for small values of the transverse magnetic field. On the other hand, the two-velocity hydrodynamic model provides an adequate explanation of the main features of the suppression of M for both paramagnetic and diamagnetic states and any values of h_0.

I. INTRODUCTION

The electrodynamics of hard superconductors is a very complex problem if the external magnetic field changes both its modulus and direction. This problem has drawn considerable attention from many research groups for a long time. The major difficulties are connected to the specific properties of the flux-line system. It is well known that, in spite of the vortex magnetic interaction, vortices in bulk hard superconductors cannot follow the direction of the external magnetic field (see, for example, Ref. 1). Indeed, the gain in the Gibbs free energy due to the vortex system orientation along the external magnetic field is proportional to the length L of the vortex, whereas the work against pinning forces is proportional to the second power of L. The same result can easily be obtained by comparing the inflecting torque acting on a straight vortex, which is created by the magnetic field, with the retaining torque of the homogeneous pinning force. The former is proportional to the vortex length L. Being proportional to L^2, the latter is much higher than the first one. Nevertheless, the magnetic field torque can bend vortices near the sample edges. This bending occurs only in finite regions near the edges where there is penetration of the transverse component $H\sin(\alpha)$ of the external magnetic field $\vec{H}$ (here α is the angle between $\vec{H}$ and the vortex). The length of this region is of the order of $cH\sin(\alpha)/4\pi J_c$,[2] which is a marginal amount for long samples (J_c is the critical current density).

To describe the behavior of hard superconductors in a rotating magnetic field, many authors[3–11] took into account an important physical phenomenon called flux-line cutting.[4,5,12–17] Only by this phenomenon can vortices change their orientation. The double critical-state model for the description of the electrodynamics of hard superconductors was proposed theoretically in Ref. 18 and developed in Ref. 19. This model is based on the concepts of both flux-line cutting and flux-line pinning. It allows the explanation of many interesting experimental results in classical[3,9,10,20–22] and high-T_c (Refs. 23–27) superconductors. The large num-

ber of examinations and verifications of this model apparently provides evidence that the problem of the description of hard superconductors placed in a magnetic field changing its direction has been completely exhausted. However, there exist some experimental facts which are rather difficult to interpret within the double critical-state model.[1,28–37] The common feature of the phenomena observed in these papers is the suppression of a dc shielding current inside all spatial regions where the penetration of an ac transverse magnetic field is observed. For example, the effect of a sweeping transverse magnetic field (later we shall denote this field as H_y) on the static magnetic moment M_z caused by a longitudinal dc magnetic field H_z was studied in Refs. 32, 34, and 37. The suppression of M_z was observed in the cases $H_y \ll H_z$ and $H_y \sim H_z$. To explain the observed phenomena a theoretical approach inspired by the double critical-state model was developed in Refs. 1, 37, and 38. In comparison with the Clem–Pérez-González model, this approach takes into account the influence of the flux-line cutting on the condition of force balance for the vortex system. This model (called the two-velocity hydrodynamic model) predicts the existence of different spatial zones inside the superconductor. In one of them, the collapse zone, the modulus of the magnetic induction $B(x)$ turns out to be homogeneous. There is also another zone, the Clem zone, where the spatial distribution of $\vec{B}$ is described by the model developed in Ref. 18.

In this paper we present an experimental investigation of the phenomenon of the static magnetic moment M_z suppression by the sweeping transverse magnetic field H_y. We measure the dependence $M_z(H_y)$ obtained under various conditions for different samples. These results are presented in Sec. II. All experimental data are discussed in Sec. III within the framework of the double critical-state model (Sec. III A) and the two-velocity hydrodynamic one (Sec. III B). The main equations of both models are presented at the beginning of the corresponding subsections. Theoretical results obtained for the dependence $M_z(H_y)$ on the basis of the two-velocity hydrodynamic model are consistent with experimental ones. Different scenarios of the evolution of the collapse zone and the Clem zone when the transverse magnetic field H_y increases are studied numerically (see Appendix B).

II. EXPERIMENT

A. Experimental procedure

To study the effect of an ac magnetic field on the static magnetization of hard superconductors, we have used a number of platelike melt-textured $YBa_2Cu_3O_{7-\delta}$ samples prepared by different technological groups. The plates were cut off from the homogeneous part of melt textured ingots in such a way that the largest faces of these slabs were parallel to the **ab** crystallographic plane. Most of the data discussed in this paper have been obtained for samples A98 and G21 with sizes of $8\times5\times0.21$ mm^3 and $8.3\times4\times0.4$ mm^3, respectively. The critical temperature of both samples was above 90 K and the width of the transition was as small as 0.5 K. We also made measurements on a large hexagonal single crystal $YBa_2Cu_3O_{7-\delta}$ provided by Donglu Shi at the University of Cincinnati and John R. Hull at Argonne National Laboratory. This crystal has a diagonal length 2.2 cm and thickness 0.9 cm along the **c** axis.

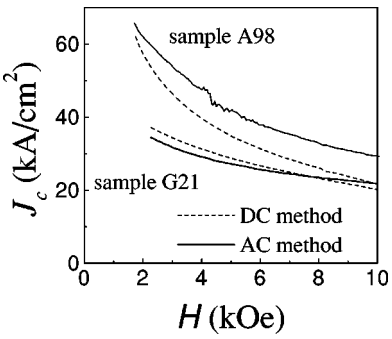

FIG. 1. The critical current density $J_c^{\perp}$ vs the magnetic field $\mathcal{H}$ estimated from magnetization loops (dashed curves) and from measurements of the ac magnetic susceptibility (solid curves) for samples A98 and G21.

The measurements of the magnetization M_z were performed by two methods. In the first approach, M_z was monitored using a vibrating sample magnetometer (VSM) with a vibrating frequency of 83 Hz and vibrating amplitude of 0.4 mm. The dc magnetic field $\vec{\mathcal{H}}=\{0,0,H_z\}$ with the strength up to 12 kOe and the spatial nonuniformity in the sample region as low as 0.1% was created by an electromagnet. The samples were mounted so that $\vec{\mathcal{H}}$ was parallel to its surface (the **yz** plane). The sweeping field $h(t)$ was induced by an additional solenoid. The sample was located in its central homogeneous field zone. The magnetic field $\vec{h}(t)=\{0,H_y(t),0\}$ was strictly parallel to the sample surface and orthogonal to the dc field $\vec{\mathcal{H}}$. The field $\vec{h}(t)$ was directed along the longest dimension of the samples. The sweeping fields had a triangular pulse form with the amplitude h_0 of up to 1000 Oe.

We also used another procedure to measure the magnetic moment M_z. A single layer 38 B&S manganin wire electric heater was intimately and noninductively (bifilarly) wound around the large single crystal. A 10 000–turn pickup coil embraced the crystal and was series opposition connected to a balancing coil of the same area and number of turns which did not ''see'' the sample but was permeated by $\vec{\mathcal{H}}$. The signal from this pickup coil ''pair'' fed an electronic amplifier integrator which drove the Y axis of an X-Y recorder. The X axis was driven by the voltage across calibrated shunts placed in the circuits of the solenoid generating $\vec{\mathcal{H}}$ or of a rectangular coil embracing the length of the solenoid and generating $h(t)$. Consequently, M_z could be continuously monitored as either $\mathcal{H}$ or h was impressed and varied. M_z was calibrated assuming perfect shielding in the linear weak-field regime when $\mathcal{H}$ was impressed after zero-field cooling. Measurements were done at liquid nitrogen temperature $T=77$ K and at $T\approx83$ K.

The critical current density, J_c, in samples A98 and G21 was estimated using the magnetization loops, $M_z(\mathcal{H})$, in zero ac field $h=0$. Our evaluation gives the $J_c(\mathcal{H})$ dependences shown in Fig. 1 by dashed curves. We have also compared these findings with the results obtained by measuring the ac magnetic susceptibility. The ac technique and the method of J_c calculation were described in Ref. 39. According to this

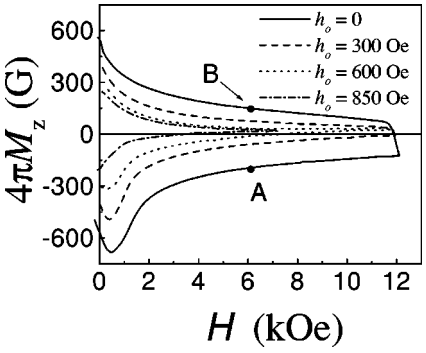

FIG. 2. The suppression of the magnetization loops $M_z(\mathcal{H})$ for sample A98 by the ac magnetic field with different amplitudes: $h_0 = 0$ (solid curve), 300 Oe (dashed curve), 600 Oe (dotted curve), and 1000 Oe (points). Only the right halves of the magnetization loops are shown.

paper, the imaginary part of the ac magnetic susceptibility, $\chi''(\mathcal{H})$, of a superconducting plate in the dc field $\mathcal{H}$ and the probe ac field with the amplitude $\tilde{h}$ (both parallel to the z axis) is related to the critical current density $J_c(\mathcal{H})$ by the equation

$$J_c(\mathcal{H}) = \begin{cases} (4c\tilde{h}/9\pi d)\chi''_{max}/\chi''(\mathcal{H}), & \mathcal{H} < H_1, \\ (3c\tilde{h}/8\pi d)\{1 \pm [1-\chi''(\mathcal{H})/\chi''_{max}]^{1/2}\}, & \mathcal{H} > H_1. \end{cases} \quad (1)$$

Here H_1 is the value of the magnetic field $\mathcal{H}$ where the probe ac field penetrates the whole sample, the plus sign in Eq. (1) is used in the region $\mathcal{H} < \mathcal{H}_m$, and the minus sign corresponds to fields $\mathcal{H} > \mathcal{H}_m$, where $\mathcal{H}_m$ is the field at the maximum of $\chi''(\mathcal{H})$. A simple way to define the value of H_1 is by the relation $\chi''(H_1) = (8/9)\chi''_{max}$. The $J_c(\mathcal{H})$ curves calculated from these data are represented by solid lines in Fig. 1. The magnetic field dependence of the critical current density for both samples A98 and G21 can be approximately described by a power function with an exponent ≈ -0.3. The characteristic value of J_c is a few tens of kA/cm^2.

The magnetic field dependence of J_c can be evaluated also by measuring the full penetration and double penetration fields H_p and H_p^*. The full penetration field H_p was determined by measuring the growth of the thermoremanent magnetization M_{zrem} as a function of $\mathcal{H}$ present during field

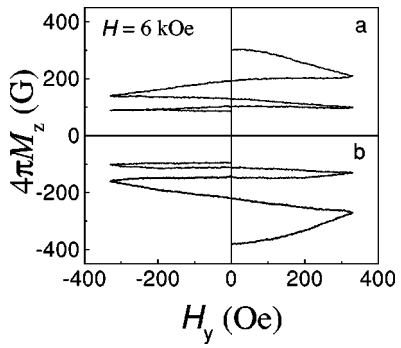

FIG. 3. The dependence of M_z on the initial cycles of the transverse magnetic field $h(t)$. Results are obtained for sample G21, $\mathcal{H} = 6$ kOe. Curves (a) and (b) correspond to the paramagnetic and diamagnetic cases, respectively.

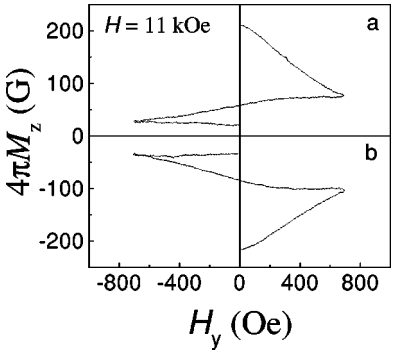

FIG. 4. The dependence of M_z on the initial cycles of the transverse magnetic field $h(t)$. Results are obtained for sample G21, $\mathcal{H} = 11$ kOe. Curves (a) and (b) correspond to the paramagnetic and diamagnetic cases, respectively.

cooling. The field $\mathcal{H}$ which leads to the maximum M_{zrem} corresponds to H_p. This quantity was also determined, although less accurately, by noting the field $\mathcal{H}$ where the initial (zero-field-cooled) magnetization curve merges with the hysteresis loop. These measurements yield $H_p = 1850$ Oe and 950 Oe at 77 K and 83 K for the single crystal. The double penetration field H_p^* was determined by measuring the growth of the isothermoremanent magnetization as a function of the to and fro sweep of $\mathcal{H}$ after zero-field cooling. The field sweep which generates the maximum remanent M_z corresponds to H_p^*. These measurements gave $H_p^* = 3300$ Oe and 1700 Oe at 77 K and 83 K. The critical-state model, taking $J_c \propto \mathcal{H}^{-n}$, leads to $(H_p^*/H_p)^{n+1} = 2$; hence $n \approx 0.2$ for the single crystal. This value for n is in harmony with the structure of the magnetization envelopes.

B. Experimental results

The dependence of the magnetic moment M_z on the transverse magnetic field h was studied for two main starting points on the static magnetization curve. These positions are schematically shown in Fig. 2 by points A and B. The point A corresponds to the diamagnetic branch of this curve. Later we shall call such a starting position as the diamagnetic branch or diamagnetic case. Position B corresponds to a paramagnetic portion of the magnetization curve. We shall call such a starting condition as the paramagnetic case.

The typical dependence of the longitudinal magnetic moment M_z on the transverse sweeping magnetic field $H_y = h(t)$ is presented in Figs. 3–5. The main feature of all these curves is an essential suppression of the magnetic moment under the action of the field $h(t)$. It is a striking fact that the magnetic moment M_z is suppressed by more than half after a rotation of the external magnetic field $\vec{H}$ through only 3° (see Figs. 3 and 4). We consider this suppression using as an example curve (a) in Fig. 3 which corresponds to a paramagnetic branch of M_z. It is remarkable that the noticeable suppression of M_z occurs for each quarter-period of the change of the sweeping field. The strongest suppression is observed for the first quarter-period. We draw attention to the fact that a similar suppression takes place for the diamagnetic branch of M_z as well [see curve (b)]. The phenomenon is strongly pronounced not only at $h \sim \mathcal{H}$ (Fig. 5) but even in the case $h \ll \mathcal{H}$ (Figs. 3 and 4).

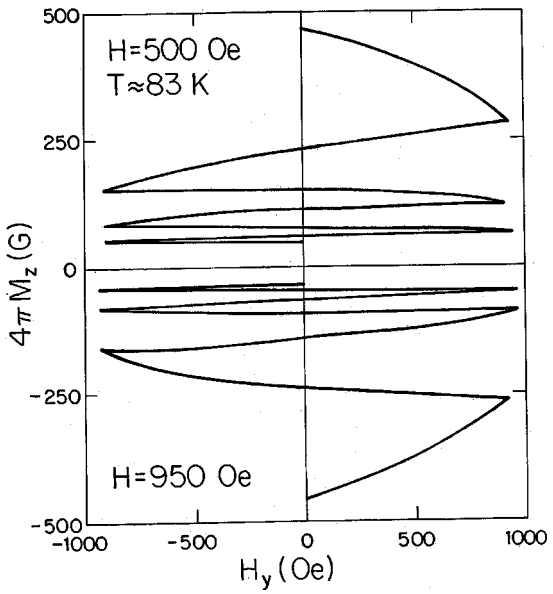

FIG. 5. Illustrates the dependence of M_z for the large hexagonal YBCO single crystal on the initial cycles of the transverse magnetic field $h(t)$. $\mathcal{H}$ and $h(t)$ were applied along the flat surfaces of the hexagonal crystal, hence $\perp$ to the **c** axis, with $h(t)$ directed along a diagonal length. Each full cycle spans several seconds. The behavior displayed here was observed at 77 K and 83 K with M_z situated along either the diamagnetic or paramagnetic critical-state envelopes of the hysteresis curves over the range $\mathcal{H} \leqslant 1200$ Oe where the field of the copper wire wound solenoid remained constant throughout the cycles of $h(t)$. At 83 K each half-cycle diminishes $|M_z|$ more effectively for a chosen amplitude h_0 than at 77 K since $h_0/H_p \approx 1$ at 83 K while $h_0/H_p \approx 1/2$ at 77 K. Application of several (i.e., $\geqslant 10$) cycles at 83 K diminished $|M_z|$ to near zero in all cases but did not lead to any reversal of the sign of the residual magnetization.

Note that the shape of $M_z(h)$ curves depends on the experimental conditions. There exist two kinds of $M_z(h)$ dependence. To demonstrate this, let us consider for the sake of definiteness the curves (b) in Figs. 3, 4, and 5 related to the diamagnetic branches of M_z. The difference between these curves is most pronounced for the first quarter-period of the change of $h(t)$. The first portions of curve (b) in Fig. 3 and the curve in Fig. 5 are bulging downward whereas the corresponding portion in Fig. 4 is mostly bulging upward. The analogous difference is observed for the paramagnetic branches of M_z.

III. DISCUSSION

The aim of this section is the comparison of the experimental data with the results of calculations of the magnetic moment suppression under the action of the transverse magnetic field within two established theoretical models. One of them is the well-known double critical-state model, which was formulated in its final form in Ref. 18. The second model, suggested in Refs. 1, 37, and 38, provides a more detailed description of the vortex system behavior in crossed ac and dc magnetic fields. Unfortunately, both models do not account for all features of very complex vortex dynamics. In addition, they contain a number of intrinsic parameters some of which are difficult to measure. Both models can pretend to a qualitative description of the phenomenon, and we will therefore compare the theoretical and experimental results qualitatively. We will study the different scenarios of the evolution of the vortex system under the change of the transverse magnetic field.

A. Double critical-state model

1. Main equations of the model

The double critical-state model was suggested by Clem and Pérez-González to generalize the well-known Bean critical-state model for the case where the external magnetic field changes not only in its modulus but in direction as well. According to this model, the gradient of the modulus B of the magnetic induction as well as the gradient of the tilt angle ϑ of $\vec{B}$ with respect to the z axis, chosen arbitrarily in the sample plane, cannot exceed certain corresponding critical values.

The double critical-state model for a plane superconducting sample of thickness d operates with the following set of equations for the spatial distributions of the modulus of the magnetic induction $\vec{B}(x)$ and the tilt angle $\vartheta(x)$. The first four equations are the usual Maxwell equations with the displacement current being neglected:

$$\frac{\partial B}{\partial x} = -\frac{4\pi}{c} J^{\perp}, \quad B\frac{\partial \vartheta}{\partial x} = \frac{4\pi}{c} J^{\parallel}, \tag{2}$$

$$E^{\perp}\frac{\partial \vartheta}{\partial x} - \frac{\partial E^{\parallel}}{\partial x} = -\frac{1}{c} B\frac{\partial \vartheta}{\partial t}, \quad \frac{\partial E^{\perp}}{\partial x} + E^{\parallel}\frac{\partial \vartheta}{\partial x} = -\frac{1}{c}\frac{\partial B}{\partial t}. \tag{3}$$

Here E is the electric field, J is the current density; signs $\perp$ and $\parallel$ denote vector components across and along the magnetic induction $\vec{B}(x)$, respectively. The double critical-state model also involves the material equations which can be written as follows:

$$E^{\perp} = \begin{cases} \rho^{\perp}[|J^{\perp}| - J_c^{\perp}(B)]\mathrm{sgn}(J^{\perp}), & |J^{\perp}| > J_c^{\perp}, \\ 0, & 0 \leqslant |J^{\perp}| \leqslant J_c^{\perp}, \end{cases} \tag{4}$$

and

$$E^{\parallel} = \begin{cases} \rho^{\parallel}[|J^{\parallel}| - J_c^{\parallel}(B)]\mathrm{sgn}(J^{\parallel}), & |J^{\parallel}| > J_c^{\parallel}, \\ 0, & 0 \leqslant |J^{\parallel}| \leqslant J_c^{\parallel}. \end{cases} \tag{5}$$

Here $J_c^{\perp}$ and $J_c^{\parallel}$ are the critical current densities, across and along $\vec{B}$, respectively; $\rho^{\parallel}$ and $\rho^{\perp}$ are effective flux-flow and flux-line-cutting specific resistivities. The current $J_c^{\perp}$ is related to flux-line pinning whereas the current $J_c^{\parallel}$ is defined by the threshold angle of the flux-line cutting. Both quantities are considered as independent phenomenological parameters. The boundary conditions consist in the equality of the magnetic induction on both surfaces of the sample to the external magnetic field, $\vec{B}(x=-d/2) = \vec{B}(x=d/2) = \vec{H}$.

2. Correlation of the experimental results with the double critical-state model

We performed numerical simulations of the spatial distribution of the magnetic induction $B(x)$ and the tilt angle

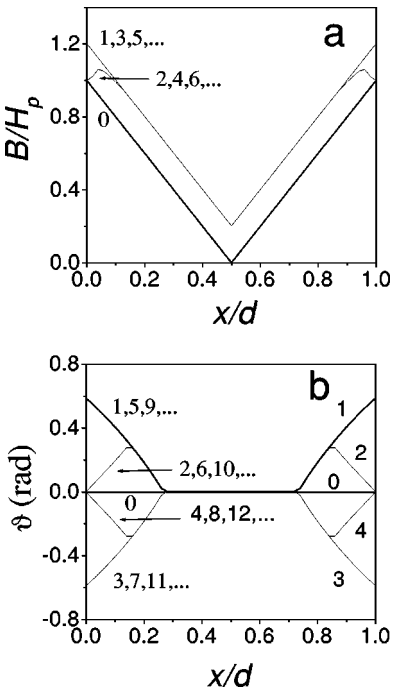

FIG. 6. The evolution of the $b(\xi)$ (a) and $\vartheta(\xi)$ (b) distributions for the diamagnetic initial state calculated within the double critical-state model for $\mathcal{H}=H_p$ with $H_p=1800$ Oe, $J_c^{\perp}=J_c^{\parallel}=3.18\times10^7$ A/m^2, and $h_0=1200$ Oe. Curves labeled 0 correspond to the initial state ($h=0$). Curves labeled 1, 2, 3, and 4 show the distributions at the ends of the first, second, third, and fourth quarter-periods of the field $h(t)$, respectively.

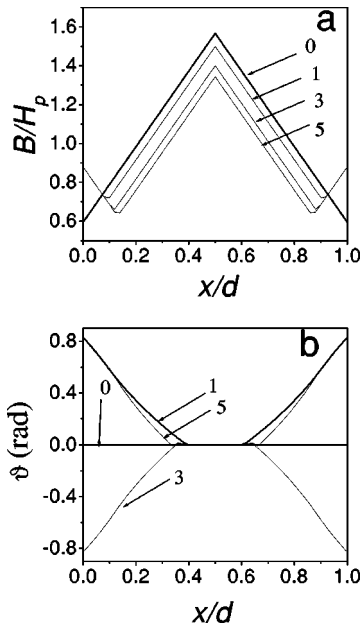

FIG. 7. The evolution of the $b(\xi)$ (a) and $\vartheta(\xi)$ (b) distributions for the paramagnetic initial state calculated within the double critical-state model for $\mathcal{H}=0.6H_p$ with $H_p=1800$ Oe, $J_c^{\perp}=J_c^{\parallel}=3.18\times10^7$ A/m^2, and $h_0=1200$ Oe. Curves labeled 0 correspond to the initial state ($h=0$). Curves labeled 1, 3, and 5 show the distributions at the ends of the first, third, and fifth quarter-periods of the field $h(t)$, respectively.

$\vartheta(x)$ for the parameters close to the experimental conditions. Additionally, we carried out the numerical calculation of the change of the z component of the magnetic moment,

$$M_z=\frac{1}{4\pi d}\int_{-d/2}^{d/2}dx[B_z(x)-\mathcal{H}], \tag{6}$$

in the process where the transverse magnetic field $h(t)$ is swept in cycles between the values $(-h_0,h_0)$. Several model samples with different thickness d and critical current density $J_c(B)$ were considered. Below we present results for two samples with $d=0.3$ mm and 9 mm, the critical current densities $J_c^{\perp}(B)=(5\times10^4)[1+B/2\times10^3\text{Oe}]^{-1/2}$ A/cm^2 and 3.18×10^3 A/cm^2, and the penetration fields $H_p=850$ Oe and 1800 Oe, respectively. The parallel critical current densities $J_c^{\parallel}(B)$ were assumed to be equal to the corresponding values of $J_c^{\perp}(B)$.

The first stage of our simulation was carried out for the model sample with thickness 9 mm and $h_0=1200$ Oe. The calculated evolution of the spatial distributions of the modulus of the magnetic induction $B(x)$ and the tilt angle $\vartheta(x)$ for the diamagnetic branch of the static magnetization curve is presented in Fig. 6. Here and below all distributions $B(x)$ and $\vartheta(x)$ are presented in dimensionless units $\xi=x/d$ and $b=B/H_p$. Curves labeled 0 in this figure correspond to the initial distributions of $b(\xi)$ (a) and $\vartheta(\xi)$ (b) before the transverse magnetic field $h(t)$ was switched on. The angle $\vartheta(\xi)$ is equal to zero everywhere, and the profile of the modulus of the magnetic induction $b(\xi)$ is linear since $J_c^{\perp}$ is assumed to be independent of B for the model sample with $d=9$ mm. When the field $h(t)$ grows, the vortices with nonzero angles begin their penetration into the sample and the distributions $B(\xi)$ and $\vartheta(\xi)$ change as well. The picture of these changes is demonstrated by the sequences of curves in Fig. 6. Curves 1 show the profiles $b(\xi)$ (a) and $\vartheta(\xi)$ (b) for the case when the transverse magnetic field $h(t)$ reaches its first maximum value h_0 (the end of first quarter-period). The distribution of $b(\xi)$ is seen to preserve the diamagnetic profile but the magnitude of b becomes higher. The reason is the increase of $B=H=(\mathcal{H}^2+h_0^2)^{1/2}$ on the surface of the sample. The region where the vortices with new orientation have penetrated corresponds to spatial intervals in Fig. 6(b) with $\vartheta\neq0$. Naturally, this region expands for higher h_0. Curves 2 in Fig. 6 correspond to the subsequent $h(t)=0$ (the end of second quarter-period). When $h(t)=-h_0$ (the end of third quarter-period) B is again a maximum at the sample surface [curve 3 of (a)] but $\vartheta(\xi)$ has reversed sign and curve 3 in (b) is the image of curve 1. In the following quarter-periods both $b(\xi)$ and $\vartheta(\xi)$ change periodically [the distributions $b(\xi)$ and $\vartheta(\xi)$ at the ends of each quarter-period repeat one of the previous profiles as indicated by the sequences of numbers in Fig. 6]. These periodic changes are reminiscent of the well-known behavior of the distribution $b(\xi)$ in the usual Bean critical-state model.

The evolution of the profiles of $b(\xi)$ and $\vartheta(\xi)$ differs essentially for the paramagnetic branch of the static magnetization curve (see Fig. 7). The initial distribution of $b(\xi)$ for this case is shown by curve 0 in Fig. 7(a). The initial angular distribution is $\vartheta(\xi)=0$ everywhere in the sample [see curve 0 in Fig. 7(b)]. The changes of the $b(\xi)$ and $\vartheta(\xi)$ profiles after the first, third, and fifth quarter-periods are demonstrated by curves 1, 3, and 5, respectively. The difference of

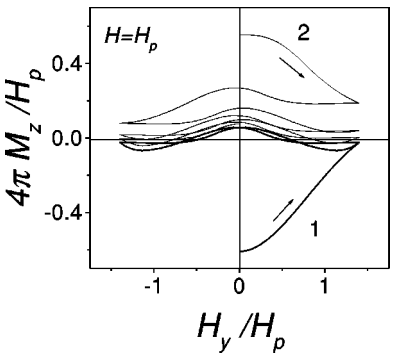

FIG. 8. The dependence of M_z on the initial cycles of the transverse magnetic field $h(t)$ calculated within the double critical-state model for $h_0/\mathcal{H}=1.4$, $\mathcal{H}=H_p=850$ Oe, $d=0.3$ mm, and $J_c^{\perp}(B)=J_c^{\parallel}(B)=5\times10^8/\sqrt{1+(B/2000\ \mathrm{Oe})}$ A/m^2. Curves 1 and 2 are obtained for the diamagnetic and paramagnetic initial states, respectively (compare with Fig. 5).

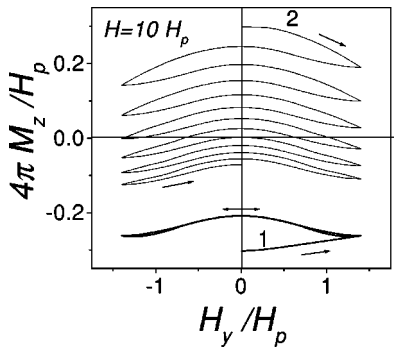

FIG. 9. The dependence of M_z on the initial cycles of the transverse magnetic field $h(t)$ calculated within the double critical-state model for $h_0/\mathcal{H}=0.14$, $\mathcal{H}=10H_p$, $H_p=850$ Oe, $d=0.3$ mm, and $J_c^{\perp}(B)=J_c^{\parallel}(B)=5\times10^8/\sqrt{1+(B/2000\ \mathrm{Oe})}$ A/m^2 as in the previous figure. Curves 1 and 2 are obtained for the diamagnetic and paramagnetic initial states (compare with Figs. 3 and 4).

the evolution of $\vartheta(\xi)$ in Fig. 7(b) from the corresponding change of $\vartheta(\xi)$ for the diamagnetic case [Fig. 6(b)] consists only in its nonperiodic behavior. The evolution of the profile $b(\xi)$ in the paramagnetic case differs substantially in comparison with the diamagnetic case. For every half-period the height of the paramagnetic triangle in the central region of the sample in Fig. 7(a) decreases. Besides, the gradient of the magnetic induction $dB(\xi)/d\xi$ changes its sign near the sample surfaces where the angle $\vartheta(\xi)\neq0$ [see Fig. 7(a)]. Therefore, the distribution $b(\xi)$ in these regions of the surface resembles the diamagnetic one, which is shown in Fig. 6(a). Thus, the paramagnetic portion of $b(\xi)$ is damped, whereas the diamagnetic region in Fig. 7(a) is enlarged, when the number n of half-periods is increased. These features of the evolution of the distributions $b(\xi)$ and $\vartheta(\xi)$ are insensitive to the sample parameters and the magnetic field dependence of the critical current density $J_c^{\perp}(B)$.

According to these results, the transition of an initial paramagnetic type of magnetization M_z to a diamagnetic one with an increase of n can be expected. We carried out a direct calculation of the dependence of the magnetic moment M_z on the initial cycles of the transverse magnetic field $h(t)$ for both the diamagnetic and paramagnetic cases. In accordance with the studied evolution of the distributions $b(\xi)$ and $\vartheta(\xi)$, the magnetic moment is essentially suppressed only during the first quarter-period and then changes periodically in the diamagnetic case (see curve 1 in Fig. 8). In contrast, in the paramagnetic case, M_z decreases step by step during every half-period and transfers to the diamagnetic state after 3 cycles (curve 2 in Fig. 8).

At first glance our calculations within the Clem–Pérez-González model agree relatively well with the experimental data. Indeed, the magnetic moment M_z is suppressed under the action of the transverse magnetic field. This suppression exists for both the diamagnetic and paramagnetic branches of the static magnetization curve. Moreover, the shapes of both curves $M_z(h)$ in the first cycle of the application of $h(t)$ are similar to the experimental ones shown in Fig. 5. However, detailed considerations reveal a pronounced disagreement with the experiments. The main contradiction consists in the asymmetric behavior of the $M_z(h)$ suppression for the diamagnetic and paramagnetic cases during subsequent cycles. In the experiments the suppression of M_z is shown to be qualitatively identical. We observed the step by step suppression after each cycle of $h(t)$ for both cases. In contrast, the calculated $M_z(h)$ curves show a step-by-step decreasing magnetic moment for the paramagnetic case only. In addition, this decrease leads to the conversion of the paramagnetic state to a brightly pronounced diamagnetic one, whereas in the experiments the magnetic moment is suppressed to a zero value approximately.

To clarify the situation, we carried out our calculations for a smaller value of h_0 compared with $\mathcal{H}$. Results of such calculations for $h_0=0.14\mathcal{H}$ are shown in Fig. 9. This figure shows an unexpected behavior of the magnetic moment. In spite of the much smaller $h_0/\mathcal{H}$ the important feature of the suppression of the paramagnetic M_z is conserved. Further, the step-by-step strong decrease of M_z proceeds until a transition into the diamagnetic state is observed. This behavior is similar to that encountered with a larger $h_0/\mathcal{H}$. In contrast with the diamagnetic case, only small suppression occurs. These results are in plain contradiction with our experiments. The suppression of the magnetic moment M_z is symmetrical for both the diamagnetic and paramagnetic cases. This can readily be verified by considering the curves displayed in Figs. 3, 4, and 5 and the magnetization loops in Fig. 2.

Thus, the double critical-state model cannot even qualitatively explain some essential features of the phenomenon under consideration. Therefore, it is necessary to invoke other ideas to describe these features. We study below the suppression of the magnetic moment by the transverse magnetic field within another theoretical model developed recently in Refs. 1, 37, and 38.

B. Two-velocity hydrodynamic model

1. Main equations of the model

The motion of the vortex system can be described in a two-component hydrodynamic approach. We assume the existence of two vortex subsystems A and B, which are characterized by the averaged tilt angles $\vartheta_A(x,t)$ and $\vartheta_B(x,t)$ with respect to the z axis, the same vortex densities $n_A(x,t)=n_B(x,t)=n(x,t)/2$, and the velocities $V_A(x,t)$ and $V_B(x,t)$, respectively. The total vortex density $n(x,t)$ is con-

nected to the magnetic induction $B(x,t)$ by the local relation $B(x,t)=\Phi_0 n(x,t)$ where Φ_0 is the magnetic flux quantum. The velocities $V_A(x,t)$ and $V_B(x,t)$ are expressed via the average hydrodynamic, $V(x,t)$, and relative, $U(x,t)$, velocities

$$V_A=V+\frac{U}{2}, \quad V_B=V-\frac{U}{2}. \tag{7}$$

The motion of the vortex system results in the change of $n(x,t)$ and $\vartheta=(\vartheta_A+\vartheta_B)/2$ which are governed by the continuity equations

$$\frac{\partial n}{\partial t}=-\frac{\partial(n\cdot V)}{\partial x}, \tag{8}$$

$$\frac{\partial(n\vartheta)}{\partial t}=-\frac{\partial}{\partial x}(n\cdot V\cdot\vartheta)+\frac{\partial}{\partial x}\left(\frac{1}{4}n\cdot|U|\cdot l\frac{\partial\vartheta}{\partial x}\right). \tag{9}$$

The vortex mean free path l represents the relation of the intervortex distance $a=n(x,t)^{-1/2}$ to the averaged probability p of the flux-line cutting at the vortice intersection. The electrodynamic equations have been derived in Refs. 1, 37, and 38 from the condition of the force balance for each of the sublattices A and B and can be presented as follows:

$$\frac{\partial B}{\partial x}=-\frac{4\pi}{c}J_c^{\perp}\,\mathrm{sgn}\,V\Theta(|V|-|U|/2),$$

$$\frac{\partial\vartheta}{\partial x}=\mathrm{sgn}\,U\left[\frac{4\pi J_c^{\perp}[p+2\Theta(|U|/2-|V|)]}{clH\cos(\vartheta-\vartheta_0)}\right]^{1/2}. \tag{10}$$

Here ϑ_0 is the angle between the external magnetic field $\vec{H}(t)$ and the z axis; $\Theta(x)$ is the Heaviside function $[\Theta(x)+\Theta(-x)=1]$. The form of this system is sensitive to the relation between the velocities $V(x,t)$ and $U(x,t)$. If $|V|>|U|/2$, then

$$\frac{\partial B}{\partial x}=-\frac{4\pi}{c}J_c^{\perp}\,\mathrm{sgn}\,V,$$

$$\frac{\partial\vartheta}{\partial x}=\sqrt{\frac{\sqrt{2}\pi}{c}J_c^{\perp}\frac{p^2n^{1/2}}{H\cos(\vartheta-\vartheta_0)}}\,\mathrm{sgn}\,U. \tag{11}$$

These equations are clearly seen to be essentially identical to those of the double critical-state model (2). In the opposite case $|V|<|U|/2$, when the sublattices A and B move in the opposite directions, the form of the electrodynamic equations changes radically:

$$\frac{\partial B}{\partial x}=0,$$

$$\frac{\partial\vartheta}{\partial x}=\sqrt{\frac{\sqrt{2}\pi}{c}J_c^{\perp}\frac{(2+p)pn^{1/2}}{H\cos(\vartheta-\vartheta_0)}}\,\mathrm{sgn}\,U. \tag{12}$$

Finally, in the case when $|V|=|U|/2$ and one of the sublattices A or B does not move the set of the equations is transformed to the following single equation:

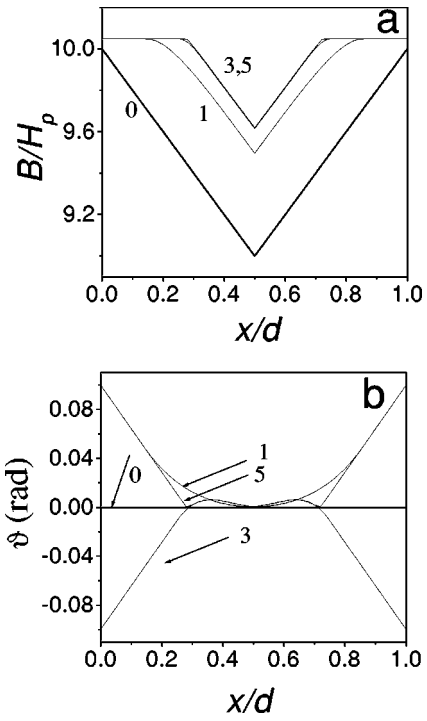

FIG. 10. The evolution of the $b(\xi)$ (a) and $\vartheta(\xi)$ (b) distributions for the diamagnetic initial state calculated within the two-velocity hydrodynamic model for $\mathcal{H}=10H_p$, $h_0=H_p$, and $p=10^{-4}$. Curves 0 correspond to the initial state ($h=0$). Curves 1, 3, and 5 show the distributions at the ends of the first, third, and fifth quarter-periods of the field $h(t)$, respectively.

$$\frac{\partial B}{\partial x}-\frac{\sqrt{2}H}{pn^{1/2}}\left(\frac{\partial\vartheta}{\partial x}\right)^2\cos(\vartheta-\vartheta_0)\,\mathrm{sgn}\,V$$
$$=-\frac{4\pi}{c}J_c^{\perp}\left(1+\frac{p}{2}\right)\mathrm{sgn}\,V. \tag{13}$$

In obtaining Eqs. (11)–(13) from Eq. (10) we used $l=2\sqrt{2}/p\sqrt{n}$.[38]

2. Correlation of the experimental results with the two-velocity hydrodynamic model

The evolution of the distributions of $b(\xi)$ and $\vartheta(\xi)$ calculated for the diamagnetic case within the two-velocity hydrodynamic model is shown in Figs. 10(a) and 10(b), respectively. Details of the calculation are given in Appendix A. Here and below this calculation was done for a model sample 4 mm thick and magnetic field $H_p=1000$ Oe. Other parameters for this figure are $\mathcal{H}=10H_p$, $h_0=H_p$, and $p=10^{-4}$. Curves 0, 1, 3, and 5 correspond to the initial distribution and the ends of the first, third, and fifth quarter-periods of the change of $h(t)$, respectively. The characteristic feature of curves 1, 3, and 5 for $b(\xi)$ is the existence of flat sections where $db/d\xi=0$. The size of those portions grows with the number of half-periods. We call the collapse zones the regions where the modulus of the magnetic induction is homogeneous, since the component of the shielding current density orthogonal to $\vec{B}$ disappears owing to the interaction of the sublattices A and B. In accordance with Eq. (12), these sublattices move in opposite directions during the

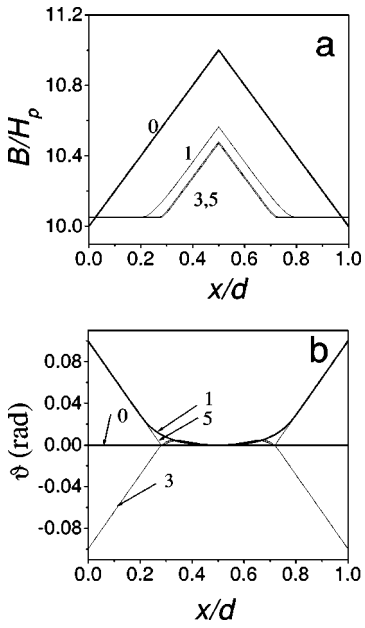

FIG. 11. The evolution of the $b(\xi)$ (a) and $\vartheta(\xi)$ (b) distributions for the paramagnetic initial state calculated within the two-velocity hydrodynamic model for $\mathcal{H}=10H_p$, $h_0=H_p$, and $p=10^{-4}$. Curves 0 correspond to the initial state ($h=0$). Curves 1, 3, and 5 show the distributions at the ends of the first, third, and fifth quarter-periods of the field $h(t)$, respectively.

change of the transverse field $h(t)$. Besides the collapse zones, there exists the central part of the sample where $db/d\xi \neq 0$. The Clem-like equations (11) are satisfied in this region, and we call it the Clem zone. According to Eqs. (11), such a zone is characterized by the motion of the vortex sublattices A and B in the same direction.

The evolution of the magnetic induction distribution $\vec{B}(x)$ for the paramagnetic case at the same conditions is displayed in Fig. 11. This evolution is very similar to that in the diamagnetic case. The changes of the $b(\xi)$ and $\vartheta(\xi)$ distributions lead to approximately symmetrical suppression of the magnetic moment M_z in both the diamagnetic and paramagnetic cases. This is demonstrated by the curves in Fig. 12 obtained for the same parameters as in Figs. 10 and 11. The

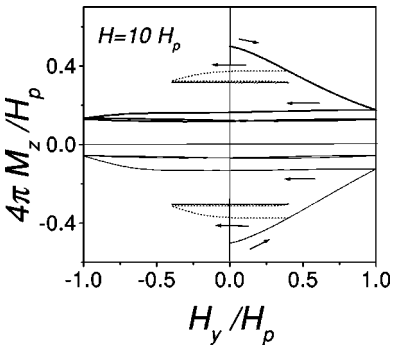

FIG. 12. The dependence of M_z on the initial cycles of the transverse magnetic field $h(t)$ calculated within the two-velocity hydrodynamic model for $h_0/\mathcal{H}=0.1$ (solid line) and $h_0/\mathcal{H}=0.04$ (dotted line) with $p=10^{-4}$. Upper and lower curves are obtained for the diamagnetic and paramagnetic initial states, respectively (compare with Figs. 3, 4, and 5).

solid and dotted lines correspond to $h_0=H_p$ and $h_0=0.4H_p$, respectively. Noticeable damping of M_z occurs in spite of relatively small amplitudes h_0 with respect to the dc field $\mathcal{H}$. This result agrees with the experimental data in Figs. 3 and 4.

Thus, the main features of the suppression of the magnetic moment M_z under the action of the transverse magnetic field are adequately described within the framework of the two-velocity hydrodynamic model. In Appendix B, we analyze some predictions of this model for the evolution of the Clem zone and the collapse zone as the transverse magnetic field $h(t)$ is increased.

IV. CONCLUSION

We have studied the nontrivial phenomenon of the strong suppression of the static magnetic moment of a hard superconductor by a transverse magnetic field. A remarkable decrease of M_z even for small orthogonal field $h(t)$ was observed and discussed within two established theoretical models. The first of these is the double critical-state model proposed by Clem and Pérez-González. This model comprises important features of the flux-line lattice behavior, namely, the flux-line cutting and the flux-line pinning. The Clem–Pérez-González electrodynamic model is based on similar insights as the Bean critical-state model. It takes into account the condition of the balance of force as the usual critical-state model and an additional condition related to the existence of a threshold angle for the flux-line cutting. This double critical-state model allows one to interpret some features of the discussed phenomenon. In particular, it describes qualitatively the collapse of the magnetic moment M_z for relatively large amplitudes of the transverse magnetic field during the first half-period of the orthogonal field $h(t)$. However, contrary to our experimental data, the results of calculations obtained using this model show an asymmetric decrease of M_z for the diamagnetic and paramagnetic initial states. The calculated suppression of M_z occurs only during the first quarter-period of the change of $h(t)$ for the diamagnetic initial state while the moment decreases step by step after every quarter-period in the paramagnetic case. This asymmetry is more pronounced at small amplitudes of h_0 with respect to the dc field $\mathcal{H}$. The moment M_z is not very sensitive to the transverse field in the diamagnetic initial case whereas it decreases significantly, changes sign, and obtains a noticeable negative value in the paramagnetic initial case if $H_p < h_0 \ll \mathcal{H}$. These predictions of the double critical-state model are in sharp contradiction with the experiment. In other words, this model cannot describe the total collection of the experimental results even qualitatively for small h_0.

The two-velocity hydrodynamic model developed recently is shown to allow a qualitative interpretation of the complete picture of the static magnetic moment suppression by the transverse magnetic field. This model provides a more detailed description of the flux-line lattice dynamics. In particular, it accounts for the change of the condition of the force balance due to the flux-line cutting process. According to the experiment, the curves calculated within this model show symmetrical suppression of the magnetic moment for the diamagnetic and paramagnetic initial states both at large and small values of h_0. The two-velocity hydrodynamic

model predicts different scenarios of the evolution of the distribution of the magnetic induction $\vec{B}$ with the increase of $h(t)$. In some cases as is shown in Appendix B this distribution has an unusual specific form. The observation of such kinds of distribution by direct measurements would be of considerable interest.

ACKNOWLEDGMENTS

This work has been done as a part of the Russian National Program in Superconductivity, Project Nos. 100292 and 100199, and was supported by INTAS and Basic Science Foundation of Russia grants, Project Nos. IR-97-1394 and 00-02-17145.

APPENDIX A

Here we will show the procedure for solving the system of equations for $B(x,t)$ and $\vartheta(x,t)$ within the two-velocity hydrodynamic model, i.e., Eqs. (8), (9), and (10). Although the latter equations (10) are very compact, their solution turns out to be a difficult task. It is more convenient to write them in terms of the velocities V_A and V_B as[38]

$$\frac{\partial B}{\partial x} = -\frac{2\pi}{c} J_c^{\perp}[F(V_A)+F(V_B)], \tag{A1}$$

$$\frac{2\sqrt{2}H}{pn^{1/2}}\cos(\vartheta-\vartheta_0)\left(\frac{\partial\vartheta}{\partial x}\right)^2 \operatorname{sgn}\left(\frac{\partial\vartheta}{\partial x}\right) = \frac{4\pi}{c} J_c^{\perp}\left[F(V_A)-F(V_B)+p\,\operatorname{sgn}\left(\frac{\partial\vartheta}{\partial x}\right)\right], \tag{A2}$$

where the function

$$F(v)=\operatorname{sgn}^*(v). \tag{A3}$$

These equations are straightforwardly obtained by using Eqs. (34), (35), and (36) of Ref. 38 with $l=2\sqrt{2}/p\sqrt{n}$, and assuming, without loss of generality, $\vartheta_A-\vartheta_B<0$. Let us remark that the function $\operatorname{sgn}^*(v)$ coincides with $\operatorname{sgn}(v)$ everywhere except at $v=0$, where $\operatorname{sgn}^*(0)$ lies within the interval $(-1,1)$.[38]

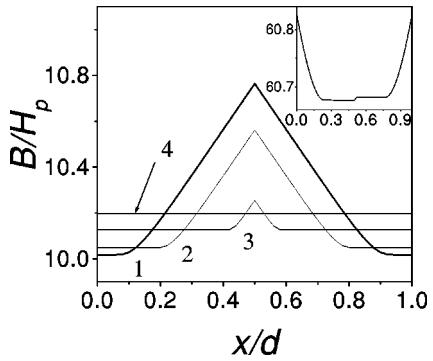

FIG. 13. The evolution of the $b(\xi)$ distribution at the end of the first quarter-period with the increase of h_0 for the paramagnetic initial state calculated within the two-velocity hydrodynamic model for $\mathcal{H}=10H_p$, $p=10^{-4}$. Curves 1, 2, 3, and 4 correspond to the $h_0/H_p=0.6$, 1.0, 1.6, and 2, respectively. The inset shows the analogous distribution for $h_0/H_p=60$.

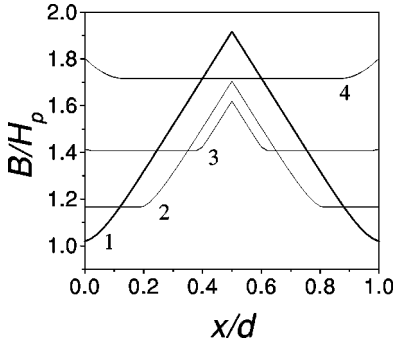

FIG. 14. The evolution of the $b(\xi)$ distribution at the end of the first quarter-period with the increase of h_0 for the paramagnetic initial state calculated within the two-velocity hydrodynamic model for $\mathcal{H}=H_p$, $p=10^{-3}$. Curves 1, 2, 3, and 4 correspond to the $h_0/H_p=0.2$, 0.6, 1.0, 1.5, respectively.

The system of equations for the two-velocity hydrodynamic model can be solved by using, instead of Eq. (A3), a relation between the variables v and F given by the expression

$$v=\begin{cases}\nu[|F|-1]\operatorname{sgn}(F), & |F|>1,\\ 0, & 0\leqslant|F|\leqslant 1.\end{cases} \tag{A4}$$

Indeed, substituting Eqs. (A1), (A2), and (A4) into Eqs. (8) and (9), we obtain a pair of coupled nonlinear equations for $B(x,t)$ and $\vartheta(x,t)$. These equations are solved numerically for slow variations of the surface boundary conditions, i.e., for small values of the velocities: $|V_A|\ll\nu$ and $|V_B|\ll\nu$. In this case the resulting spatial distributions of $B(x,t)$ and $\vartheta(x,t)$ are then practically relaxed and, in fact, independent of the auxiliary parameter ν. It should be mentioned that this method for solving the system of equations for the two-velocity hydrodynamic model is very similar to that employed to solve Eqs. (2), (3), (4), and (5) of the double critical-state model. There, the auxiliary parameters are $\rho^{\perp}$ and $\rho^{\parallel}$.

APPENDIX B

Here we shall discuss some predictions of the two-velocity hydrodynamic model. It is possible to deduce the transformation of our field distribution in the case of high

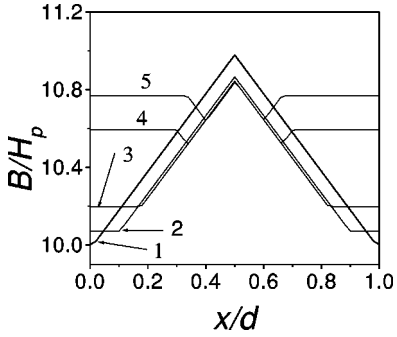

FIG. 15. The evolution of the $b(\xi)$ distribution at the end of the first quarter-period with the increase of h_0 for the paramagnetic initial state calculated within the two-velocity hydrodynamic model for $\mathcal{H}=10H_p$, $p=10^{-3}$. Curves 1, 2, 3, 4, and 5 correspond to the $h_0/H_p=0.2$, 1.2, 2.0, 3.5, 4.0, respectively.

amplitudes h_0. One should expect the appearance of the Bean-like profiles of the distribution $B_y(x)$ at $h_0 \gg H_z$, H_p. This means that the flat portions in the plots $b(\xi)$ in Fig. 10(a) should be replaced by the portions with $db/d\xi \neq 0$; i.e., the Clem zones should appear inside the sample. The simplest scenario of such evolution develops as follows. With the increase of h_0 the collapse zones enlarge and occupy the whole volume of the sample. Only after this new Clem zones appear near the surfaces of the sample. This scenario is illustrated by Fig. 13. A new Clem zone is clearly seen in the inset to that figure. The homogeneous distribution of b is displayed by curve 4.

The analysis shows that there exist other scenarios for the creation of new Clem zones. Figure 14 illustrates another scenario when the new Clem zones appear near the sample surfaces before the uniformization of the $b(\xi)$ distribution. Curves 1 and 2 show the existence of collapse zones near the surfaces of the sample and the Clem zone in the middle of the sample. The increase of h_0 leads to the appearance of new Clem zones (curve 3) and, then, to the disappearance of the central Clem zone (curve 4).

Finally, we have found another interesting scenario of transformation of the $b(\xi)$ profile. The plots corresponding to this scenario are shown in Fig. 15. Curves 1–3 demonstrate the usual initial development of the collapse zones. However, for stronger amplitudes, the new Clem zones appear in the intermediate region of the sample between its middle and the edges (curves 4 and 5). In these spatial regions, the sign of the derivative $db/d\xi$ changes after the appearance of the new zones.

[1] I. F. Voloshin, A. V. Kalinov, S. E. Savel'ev, L. M. Fisher, V. A. Yampol'skii, and F. Pérez-Rodríguez, Zh. Éksp. Teor. Fiz. **111**, 1071 (1997) [JETP **84**, 592 (1997)].

[2] K. Funaki, M. Noda, and K. Yamafuji, Jpn. J. Appl. Phys., Part 1 **21**, 1580 (1982).

[3] J. R. Cave, J. E. Evetts, and A. M. Campbell, J. Phys. (Paris), Colloq. **39**, C6-614 (1978).

[4] D. G. Walmsley, J. Phys. F: Met. Phys. **2**, 510 (1972).

[5] J. R. Clem and S. Yeh, J. Low Temp. Phys. **39**, 173 (1980).

[6] G. Fillion, R. Gauthier, and M. A. R. LeBlanc, Phys. Rev. Lett. **43**, 86 (1979).

[7] D. G. Walmsley and W. E. Timms, J. Phys. F: Met. Phys. **7**, 2373 (1977).

[8] K. Yamafuji and T. Matsushita, J. Phys. Soc. Jpn. **47**, 1069 (1979).

[9] R. Boyer and M. A. R. LeBlanc, Solid State Commun. **24**, 261 (1977).

[10] R. Boyer, G. Fillion, and M. A. R. LeBlanc, J. Appl. Phys. **51**, 1692 (1980).

[11] J. R. Clem, Phys. Rev. B **26**, 2463 (1982).

[12] A. M. Campbell and J. E. Evetts, Adv. Phys. **21**, 199 (1972).

[13] E. H. Brandt, Phys. Lett. **79A**, 207 (1980).

[14] E. H. Brandt, J. Low Temp. Phys. **39**, 41 (1980); **42**, 557 (1981); **44**, 33 (1981); **44**, 59 (1981).

[15] E. H. Brandt, J. R. Clem, and D. G. Walmsley J. Low Temp. Phys. **37**, 43 (1979).

[16] J. R. Clem, Phys. Lett. **54A**, 452 (1975); **59A**, 401 (1976).

[17] J. R. Clem, J. Low Temp. Phys. **38**, 353 (1980).

[18] J. R. Clem and A. Pérez-González, Phys. Rev. B **30**, 5041 (1984).

[19] A. Pérez-González and J. R. Clem, Phys. Rev. B **31**, 7048 (1985); **33**, 1601 (1986); **42**, 4100 (1990); **43**, 7792 (1991); J. Appl. Phys. **58**, 4326 (1985).

[20] J. R. Cave and M. A. R. LeBlanc, J. Appl. Phys. **53**, 1631 (1982).

[21] M. A. R. LeBlanc, D. LeBlanc, A. Golebiowski, and G. Fillion, Phys. Rev. Lett. **66**, 3309 (1991).

[22] M. A. R. LeBlanc and J. P. Lorrain, J. Appl. Phys. **55**, 4035 (1984).

[23] G. Gandolfini, M. A. R. LeBlanc, and J. Sekerka, Cryogenics **29**, 373 (1989).

[24] M. A. R. LeBlanc, S. Celebi, S. X. Wang, and V. Plechacek, Phys. Rev. Lett. **71**, 3367 (1993).

[25] K. V. Bhagwat, S. V. Nair, and P. Chaddah, Physica C **227**, 156 (1994).

[26] F. Pérez-Rodríguez, A. Pérez-González, J. R. Clem, G. Gandolfini, and M. A. R. LeBlanc, Phys. Rev. B **56**, 3473 (1997).

[27] A. Silva-Castillo, R. A. Brito-Orta, A. Pérez-González, and F. Pérez-Rodríguez, Physica C **296**, 75 (1998).

[28] I. V. Baltaga, L. M. Fisher, N. V. Il'in, N. M. Makarov, I. F. Voloshin, and V. A. Yampol'skii, Phys. Lett. A **148**, 213 (1990).

[29] I. F. Voloshin, N. V. Il'in, N. M. Makarov, L. M. Fisher, and V. A. Yampol'skii, JETP Lett. **53**, 115 (1991).

[30] L. M. Fisher, in *Superconductivity and Its Applications*, edited by Yi-Han Kao, Philip Coppers, and Hoi-Sing Kwok, AIP Conf. Proc. No. 219 (AIP, New York, 1991).

[31] I. V. Baltaga, L. M. Fisher, N. M. Makarov, I. F. Voloshin, and V. A. Yampol'skii, Fiz. Nizk. Temp. **21**, 411 (1995) [Low Temp. Phys. **21**, 320 (1995)].

[32] L. M. Fisher, A. V. Kalinov, I. F. Voloshin, I. V. Baltaga, K. V. Il'enko, and V. A. Yampol'skii, Solid State Commun. **97**, 833 (1996).

[33] S. K. Hasanain, Sadia Manzoor, and A. Amirabadizadeh, Supercond. Sci. Technol. **8**, 519 (1995).

[34] S. Manzoor and S. K. Hasanain, J. Phys. C **8**, 8339 (1996).

[35] S. K. Hasanain, Shaista Shahazada, and A. Mumtaz, Physica C **296**, 241 (1998).

[36] L. M. Fisher, A. V. Kalinov, S. E. Savel'ev, I. F. Voloshin, and V. A. Yampol'skii, Solid State Commun. **103**, 313 (1997).

[37] L. M. Fisher, A. V. Kalinov, S. E. Savel'ev, I. F. Voloshin, V. A. Yampol'skii, M. A. R. LeBlanc, and S. Hirscher, Physica C **278**, 169 (1997).

[38] S. E. Savel'ev, L. M. Fisher, and V. A. Yampol'skii, Zh. Éksp. Teor. Fiz. **112**, 936 (1997) [JETP **85**, 507 (1997)].

[39] L. M. Fisher, V. S. Gorbachev, N. V. Il'in, N. M. Makarov, I. F. Voloshin, V. A. Yampol'skii, R. L. Snyder, S. T. Misture, M. A. Rodriguez, D. P. Matheis, V. R. W. Amarakoon, J. G. Fagan, J. A. T. Taylor, and A. M. M. Barus, Phys. Rev. B **46**, 10 986 (1992).